



## Research Paper

# Monitoring molecular dynamics of bacterial cellulose composites reinforced with graphene oxide by carboxymethyl cellulose addition



M.J. Sanchis<sup>a,\*</sup>, M. Carsí<sup>a,b</sup>, C.M. Gómez<sup>c</sup>, M. Culebras<sup>c</sup>, K.N. Gonzales<sup>d</sup>, F.G. Torres<sup>d</sup>

<sup>a</sup> Department of Applied Thermodynamics, Institute of Electric Technology, Universitat Politècnica de València, Valencia, Spain

<sup>b</sup> Instituto de Automática e Informática Industrial, Universitat Politècnica de València, 46022 Valencia, Spain

<sup>c</sup> Departament de Química Física, Institut de Ciència dels Materials, Universitat de València, Valencia, Spain

<sup>d</sup> Department of Mechanical Engineering, Pontificia Universidad Católica del Perú, Lima 32, Peru

## ARTICLE INFO

## Article history:

Received 11 July 2016

Received in revised form

30 September 2016

Accepted 1 October 2016

Available online 4 October 2016

## Keywords:

Bacterial cellulose composites

Dielectric relaxation spectroscopy

Thermal stability

## ABSTRACT

Broadband Dielectric Relaxation Spectroscopy was performed to study the molecular dynamics of dried Bacterial Cellulose/Carboxymethyl Cellulose–Graphene Oxide (BC/CMC–GO) composites as a function of the concentration of CMC in the culture media. At low temperature the dielectric spectra are dominated by a dipolar process labelled as a  $\beta$ -relaxation, whereas electrode polarization and the contribution of dc-conductivity dominate the spectra at high temperatures and low frequency. The CMC concentration affects the morphological structure of cellulose and subsequently alters its physical properties. X-ray diffractometry measurements show that increasing the concentration of CMC promotes a decrease of the  $I_{\alpha}/I_{\beta}$  ratio. This structural change in BC, that involves a variation in inter- and intramolecular interactions (hydrogen-bonding interactions), affects steeply their molecular dynamics. So, an increase of CMC concentration produces a significantly decrease of the  $\beta$ -relaxation strength and an increase of the dc-conductivity.

© 2016 Elsevier Ltd. All rights reserved.

## 1. Introduction

New materials consisting of a biopolymer matrix reinforced with carbon derivatives (graphene and carbon nanotubes) offer interesting properties such as biodegradability and non-toxicity (Fan et al., 2010; Liu, Yu, Zeng, Miao, & Dai, 2010; Ye et al., 2016). In recent years, cellulose has been employed in various nanotechnology applications such as filtration processes or building up matrixes for microelectronic purposes (Terzopoulou, Kyzas, & Bikiaris, 2015; Miyauchi et al., 2010; Han, Yan, Chen, Li, & Bangal, 2011; Xu, Wang, Xing, Matuana, & Zhou, 2015; Feng, Zhang, Shen, Yoshino, & Feng, 2012). Few studies have been addressed to study the conductivity and energy storage of these materials but all of them conclude that there is great potential for their application in electronics development (Liu et al., 2010; Luong et al., 2011).

Cellulose is a promising alternative to the omnipresent oil-based polymers. It is produced by a diverse array of organisms: plants, bacteria, algae and even some animal species (Dayal & Catchmark, 2016; Mohite & Patil, 2016). The crystalline structure of cellulose I (native cellulose) is a mixture of two distinct crystalline forms: cel-

lulose  $I_{\alpha}$  (triclinic) and  $I_{\beta}$  (monoclinic) (Atalla & Vanderhart, 1984). The main difference between the  $I_{\alpha}$  and  $I_{\beta}$  forms is the relative displacement of cellulose sheets along their “hydrogen-bonded” planes in the direction of the chain’s axis. The directionality of the 1–4 linkage along the length of the cellulose chain affects how neighboring chains interact with each other, and thus its physical properties. The  $I_{\alpha}/I_{\beta}$  ratio have been found to vary between samples from different origins (O’Sullivan, 1977; Nishiyama, 2009). The presence of dimorphism makes it difficult to interpret XRD measurements as the positions of peaks from both crystalline forms are very close to each other. However, the cellulose sample mostly contains the crystalline form,  $I_{\alpha}$  when the intensity of the  $14.5^{\circ}$  peak is larger than that of the  $16.6^{\circ}$  peak (Lee, Gu, Kafle, Catchmark, & Kim, 2015; Tokoh, Takabe, Fujita, & Saiki, 1998).

Some bacteria from the genus *Gluconacetobacter* synthesize cellulose. This bacterial cellulose (BC) is formed by cellulose fibers (around 110 nm in diameter) that grows as a gel when cultivated in static conditions (Hirai, Yamamoto, & Hirai, 1997). The BC gel is formed by a 3D coherent network of BC fibers that provides remarkable mechanical properties, high surface area and porosity (Iguchi, Yamanaka, & Budhiono, 2000; Ul-Islam, Khan, & Park, 2012). BC-based composites have been used for a variety of applications including: membranes, strong paper, and biomaterials for

\* Corresponding author.

E-mail address: [jsanchis@ter.upv.es](mailto:jsanchis@ter.upv.es) (M.J. Sanchis).

biomedical applications (Nakagaito, Iwamoto, & Yano, 2005; Kim, Cai et al., 2011; Lin, Lien, Yeh, Yu, & Hsu, 2013).

Several works have reported the potential applications of BC-based composites in the electronic industry (Kafy, Sadasivuni, Kim, Akther, & Kim, 2015; Sadasivuni et al., 2015). Graphene oxide (GO) is among the materials used to provide cellulose-based composites with novel properties (Shao et al., 2016). GO consists of a single-layer of graphite oxide with hydroxyl and epoxy groups on the basal plane. These groups affect its electronic, mechanical, and electrochemical properties (Gómez-Navarro et al., 2010). The facile synthesis and substantial solubility of GO together with its moderate conductivity and high surface area (Chen, Feng, & Li, 2012) make it a promising material for electronic applications. Kafy (Kafy et al., 2015) prepared cellulose-GO nanocomposites by incorporating graphene oxide (GO) platelets modified with hexamethylene diisocyanate as grafting agent. The energy storage capabilities of the nanocomposites were assessed through the dielectric response of the samples. Their results showed that the dielectric constant ( $\epsilon'$ ) values increases with the GO content.

The incorporation of GO in a cellulose matrix is usually achieved by dissolving or disrupting the cellulose network to add GO platelets into a cellulose solution (Kim, Khan, Kim, Cho, & Park, 2011; Tian et al., 2014; Liu et al., 2015). In the work presented here, BC/GO composites were prepared using a bottom-up technique that preserves the 3D network structure of BC. This technique requires the modification of the BC culture medium in order to allow cellulose fibers to grow in the presence of a second phase. The viscosity of the medium must be tuned to prevent the precipitation of the second phase. Several polysaccharides including pectin, sodium alginate, and corn steep liqueur have been used to this end (Dayal & Catchmark, 2016; Gu & Catchmark, 2012).

For this investigation, we have used carboxymethylcellulose (CMC), a water-soluble semi-synthetic derivative of cellulose (Yadav, Rhee, & Park, 2013), to increase the viscosity of the culture medium and prevent the precipitation of GO platelets. GO platelets are hydrophilic and can be dispersed in the culture medium. Several studies have suggested that the hydrophilic functional groups on the surface of GO may form hydrogen bonds with the –OH groups on BC (Si et al., 2014; Feng et al., 2012; Shao, Liu, Liu, Wang, & Zhang, 2015). Previous studies show that CMC can be successfully used to suspend hydroxyapatite (HA) and starch to prepare BC/starch and BC/HA composites (Grande et al., 2009b; Grande, Torres, Gomez, & Bañó, 2009a). CMC has highly hydrophilic properties and is non-toxic, renewable, biocompatible and biodegradable (Kamarudin & Isa 2013). Several studies report that the addition of CMC into the BC culture media promotes a reduction on the diameter of BC fibers (Chen, Chen, Huang, & Lin, 2011; Huang, Chen, Lin, Hsu, & Chen, 2010; Hirai et al., 1997).

Dielectric Relaxational Spectroscopy (DRS) is one of the most versatile techniques used to examine the dynamics of polymers and small molecules (Kremer & Schönhal, 2003; Riande & Díaz-Calleja, 2004). A detailed dielectric analysis of various cellulose and derived materials has been reported by Einfeldt (Einfeldt, Meißner, Kwasniewski, Einfeldt, 2001; Einfeldt, Meißner, & Kwasniewski, 2004; Einfeldt & Kwasniewski, 2002). Due to the presence of polar molecular structures within these materials, the dielectric spectrum shows several relaxation processes. Studying dried samples, two processes with secondary relaxation character appear in the sub- $T_g$  region labelled as  $\beta$ - and  $\gamma$ -relaxations. The  $\beta$ -relaxation is dominant and related to the local backbone or segmental motion of the chain. The  $\gamma$ -relaxation is associated with the motion of the side groups of the repeating unit. The alleged primary or  $\alpha$ -relaxation, directly connected to the glass transition, is absent from cellulosic material with low moisture content. Moreover, for wet cellulosic materials a relaxation labelled as  $\beta_{wet}$  is observed in the room temperature range (Einfeldt, Meißner, Kwasniewski, 2001; Gelin et al.,

2007). This process may be associated with the collective motion of solvent-swollen cellulose regions. There is an additional process in the high temperature range, corresponding to the dc-conductivity of the sample. This relaxation is unrelated to polymer motion and is characteristic of all disordered solids with ionic conductivity.

Because of the potential interest of BC derivative materials, we have focused this paper on the analysis of the CMC content effect on the molecular dynamics of BC/CMC/GO composite samples. The BC, used in this study, was produced by the bacterium *Gluconacetobacter Xylinus*. Values of CMC were varied to evaluate their influence on thermal stability and on dynamic molecular behavior. The data will provide useful information for further development of materials derived from polysaccharides and biopolymers to be used in the electronics industry.

## 2. Experimental

### 2.1. Materials

All chemicals were of analytical grade and used without purification. Carboxymethyl-cellulose sodium salt (CMC) was procured from Acros Organics (average MW 25,0000, DS = 1.2). Graphene oxide (GO) platelets of 0.7–1.2 nm in thickness were purchased from Cheep Tubes Inc. (cat. no SKU: 060101, USA).

### 2.2. BC production

The static culture medium for the growth of BC consisted of 1.0% (w/v) D-glucose, 1.5% (w/v) peptone, 0.8% (w/v) yeast extract and 0.3% (w/v) glacial acetic acid, adjusted to 3.5 pH with hydrochloric acid. The culture medium was autoclaved at 121 °C for 20 min and then allowed to reach room temperature. Ethanol was added after sterilization to improve the growth of the cellulose gel. The strain *Gluconacetobacter Xylinus* was inoculated and cultivated at 30 °C for 21 days at room temperature.

### 2.3. BC/GO/CMC composite preparation

The viscosity of the culture medium was increased using carboxymethyl cellulose (CMC), in order to avoid the precipitation of GO platelets. CMC was added to the culture medium at concentrations of 1.0%, 2.0% and 3.0% (w/v) and stirring was carried out until CMC was completely dissolved. GO was added in concentrations of 0.01% (w/v) (Table 1). BC/CMC/GO gels were removed, washed with water, boiled in 1.0 M NaOH at 70 °C for 90 min and rinsed in deionized water. Samples were pressed in a hydraulic plate press at 105 °C to produce sheets.

### 2.4. Morphological characterization

Both scanning electron microscopy (SEM) and Atomic Force Microscopy (AFM) were employed to characterize the morphology of the samples. SEM was carried out in a Hitachi S-4800 microscope at an accelerating voltage of 20 kV and at working distance of 14 mm. Small pieces of sample was placed in the sample holder (2 inch). The samples were metalized with an Au-Pd coating before observation. Images of the surfaces of BC and BC/CMC/GO samples were carried out using AFM (easyScan 2, Nanosurf AG, Switzerland) in the tapping mode. A cantilever with a nominal spring constant of 48 N/m, resonance frequency of 190 kHz and a tip radius lower than 10 nm was used.

### 2.5. Thermal gravimetric analysis (TGA) characterization

TGA was performed using a Perkin-Elmer TGA4000 thermogravimetric analyzer. Samples weighing approximately 10–11 mg

**Table 1**  
Sample code, GO and CMC content, char residues and temperature of maximum degradation,  $T_{\max \text{ deg}}$ .

Code	GO-content (% w/v)	CMC-content (% w/v)	Char residues (%)	$T_{\max \text{ deg}}$ (°C)
BC	0	0	13	377.7
1CMC/GO	0.01	1	19	363.8
2CMC/GO	0.01	2	20	362.7
3CMC/GO	0.01	3	20	352.5

were analyzed at a heating rate of 10 °C/min from 30 ° to 700 °C under a nitrogen flow of 20 mL/min.

### 2.6. Dielectric relaxation spectroscopy (DRS) characterization

The isothermal relaxation spectra of BC/CMC/GO samples were collected with a Novocontrol Broadband Dielectric Spectrometer (Hundsagen, Germany) consisting of an Alpha Analyzer to carry out measurements from  $5 \times 10^{-2}$  to  $3 \times 10^6$  Hz. The measurements were performed in an inert  $N_2$  atmosphere from 150 °C to –150 °C. The temperature was controlled with a nitrogen jet (QUATRO from Novocontrol), with a temperature error of  $\pm 0.1$  K during each sweep in frequency. Molded disc shaped samples of about 0.12 mm thickness with diameters 10 and 20 mm were used. The thickness of each sample was measured with a micrometer screw. In order to avoid an increase of conductivity due to water, the samples were initially dried at 40 °C in a vacuum oven until constant weight was reached. In order to minimize the effect of moisture that may have been introduced during transport, the samples were heated at 150 °C and measurements were carried out from high to low temperatures. The experimental uncertainty was less than 5% in all cases.

From the several models that have been employed to characterize the isothermal relaxation spectra, the more extensively used is the empirical Havriliak-Negami (Havriliak & Negami, 1966; Havriliak & Havriliak, 1967) model (HN):

$$\varepsilon^*(\omega) = \varepsilon_\infty + \frac{\varepsilon_0 - \varepsilon_\infty}{[1 + (j\omega\tau_{HN})^{a_{HN}}]^{b_{HN}}} \quad (1)$$

where  $\varepsilon_0$  is the relaxed permittivity,  $\varepsilon_\infty$  is the unrelaxed permittivity,  $\Delta\varepsilon = \varepsilon_0 - \varepsilon_\infty$  is the strength relaxation, the parameters  $a_{HN}$  and  $b_{HN}$  [ $0 < (1 - a_{HN}), (1 - a_{HN}) b_{HN} < 1$ ] define the symmetrical and asymmetrical broadening of the loss peak respectively, and  $\tau_{HN}$  is the characteristic relaxation time. The temperature dependence of the last parameter follows the Arrhenius (ARRH) or Vogel-Fulcher-Tammann-Hesse equations (VFTH) depending of the relaxation nature.

According to the Onsager–Fröhlich–Kirkwood (OFK) equation (Fröhlich, 1959), the  $\Delta\varepsilon_\beta$  is related to the reorientation of  $N_p$  dipoles per unit volume over all spatial orientations as follows:

$$\Delta\varepsilon_\beta = \frac{\varepsilon_0(2 + \varepsilon_\infty)^2}{(2\varepsilon_0 + \varepsilon_\infty)} \frac{4\pi N_p \mu_0^2}{9k_B T} g_\beta \quad (2)$$

where  $\mu_0^2$  is the uncorrelated mean-square dipolar moment,  $k_B$  is the Boltzmann constant,  $N_p$  is the number of dipoles participating in the process and  $g_\beta$  is a factor that accounts for the intramolecular and intermolecular correlations. The term  $N_p \mu_0^2 g_\beta$  depends on the dipolar reorientation of  $N$  identical molecules per volume unit, in which each individual  $i$  has an instantaneous conformation associated with a dipole moment.

### 2.7. X-ray diffraction (XRD) characterization

Wide angle XRD measurements were carried with a Bruker AXS D5005 diffractometer. The samples were scanned at 4°/min using  $Cu K\alpha$  radiation ( $\lambda = 0.15418$  nm) at a filament voltage of 40 kV and

a current of 20 mA. The diffraction scans were collected at room temperature over the  $2\theta$  range of 5°–80° with a  $2\theta$  step of 0.01°.

Peak separations of the profiles were carried out using the non-linear least squares fitting program, where a pseudo-Voigt function was used. The  $d$ -spacings were calculated using the Bragg's equation. The crystallinity index (CrI) quantifies the relative amount of crystalline material in cellulose (Park, Baker, Himmel, Parilla, & Johnson, 2010). The CrI value varies significantly, depending on the evaluation method (Ahvenainen, Kontro, & Svedström, 2016). Segal et al. (Segal, Creely, Martin, & Conrad, 1962) estimate the CrI by means of a  $(I_{\text{cryst}} - I_{\text{am}})/I_{\text{cryst}}$  relation, where  $I_{\text{cryst}}$  is the intensity of the peak at  $2\theta$  around 22.5° and  $I_{\text{am}}$  is the intensity of the baseline at  $2\theta$  around 18°. This method usually provides exceedingly high CrI values (Park et al., 2010; Terinte, Ibbett, & Schuster, 2011; Bansal, Hall, Realf, Lee, & Bommarius, 2010). CrI can also be estimated from the ratio of the separated crystalline peak area to the total reflection area, including the background (Hermans & Weidinger, 1949; Wada & Okano, 2001).

To calculate crystal size, the Scherrer equation (Alexander, 1979) has been used

$$L = \frac{K \cdot \lambda}{FWHM \cdot \cos \theta} \quad (3)$$

where  $L$  is the crystallite size perpendicular to the plane,  $K$  is 0.94,  $\lambda$  is the X-ray wavelength,  $FWHM$  is the full-width at half-maximum in radians and  $\theta$  is the Bragg angle.

## 3. Results and discussion

### 3.1. Morphological characterization

The morphology of pure BC has been examined to compare with that of BC/CMC/GO composites with an aim to understand the effects of GO reinforcement and CMC content on the formation of the BC network. A SEM micrograph of a pure BC surface is shown in Fig. 1a. The image reveals typical fibrils around 100 nm in diameter, which coincides with data for pure BC reported previously (Grande et al., 2008) (117.76 nm). Fig. 1b shows the surface of a BC/CMC/GO composite (code 1CMC/GO), which differs significantly from the pure BC surface. The packing density of cellulose microfibrils varies significantly with the CMC addition. The diameter of the fibrils and pore size in the composite are smaller than those found in pure BC. White arrows indicate the presence of GO agglomerates in the BC/CMC/GO composite. The formation of agglomerates may be due to low dispersion, probably caused by the solution-casting method and the high surface area of GO sheets (Ebrahimzadeh, Ghanbarzadeh, & Hamishehkar, 2016).

AFM images of pure BC and BC/CMC/GO composites (code 3CMC/GO) are shown in Fig. 1c and 1d. The average diameter of pure BC fibrils is  $120.89 \pm 10.69$  nm, in agreement with the measurements reported by Grande (Grande et al., 2009a) and Bohn (Bohn, Fink, Ganster, & Pinnow, 2000). In contrast, the average diameter of fibrils grown in the presence of CMC (3%) and GO (0.01%) was  $86.72 \pm 7.93$  nm. The reduction of the BC fibrils diameter is attributed to the presence of CMC in the culture medium. This result is in agreement with previous report for BC/CMC/HAP nanocomposites (Grande et al., 2009a; Huang et al., 2010; Hirai et al., 1997).

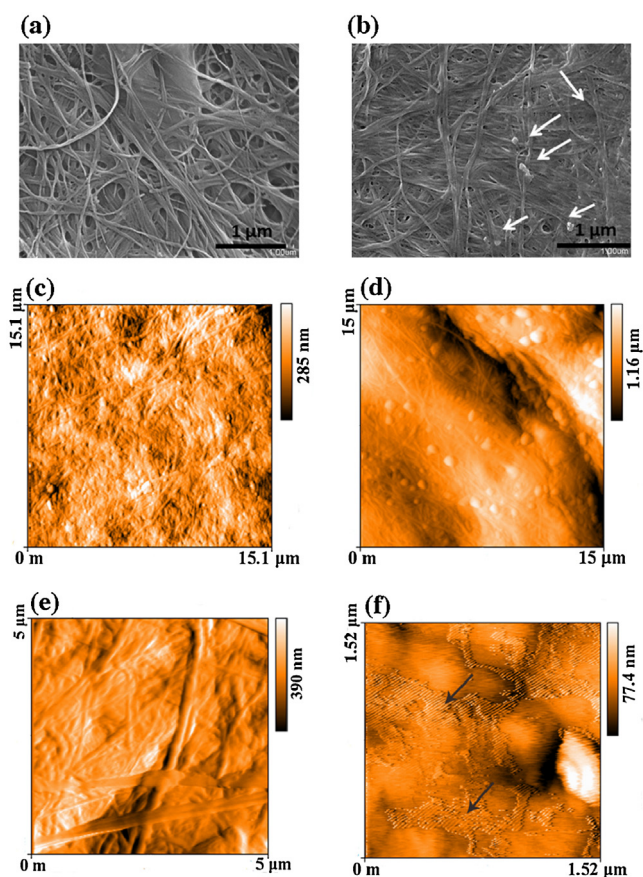


**Fig. 1.** SEM micrograph of: (a) surface of pure BC and (b) surface of BC/CMC/GO nanocomposite code 1CMC/GO. Arrows indicate agglomerates of GO within the BC matrix. AFM images depicting the topography of a representative pure BC film (c), BC/CMC-GO (sample 3CMC/GO) composite film (d) and (e). Arrows on (f) show GO agglomerates within BC sheets.

The average pore size in pure BC network meshes was  $224.4 \pm 68.35$  nm. However, for BC/CMC/GO composites it was not possible to determine consistent mesh pore sizes (Fig. 1e) since the pores in several cases appeared to be closed. The presence of GO in the composites is indicated with arrows in Fig. 1f. AFM images and SEM micrographs confirmed the presence of GO in the composites.

### 3.2. Thermal gravimetric analysis characterization

The thermal stability of the BC/CMC/GO samples was analyzed by TGA. Fig. 2a shows the TGA spectra obtained for the BC/CMC/GO samples and for CMC. Table 1 collects values of the final weight and the temperature of maximum degradation,  $T_{max\ deg}$ , of the samples. Two processes are observed: one at low temperature related to the dehydration process and another at high temperature derived from thermal degradation. The weight loss associated with the first process (around  $100^\circ\text{C}$ ) increases with the increase of CMC concentration. Thus, the CMC sample depicts a 16% weight loss, while a reduction to 5% and 6.5% is observed for BC and for the composite samples, respectively. The changes observed as a result of the CMC content appear to be linked to the hydrogen bonds present in the cellulose structure (Watanabe, Morita, & Ozaki, 2006; Watanabe, Morita, & Ozaki, 2007; Poletto, Pistor, & Zattera, 2013). In addition, the formation of hydrogen bonds between water molecules and hydroxyl groups of BC and CMC may lead to an increased retention of such water molecules in the BC composites. A second weight loss stage is observed with an onset temperature between  $290^\circ$  and  $310^\circ\text{C}$ . This temperature decreases with addition of GO and CMC.

Pure CMC has an initial decomposition temperature around  $290^\circ\text{C}$  and pure BC around  $310^\circ\text{C}$ , so BC/CMC/GO composites depict a thermogravimetric behavior between the raw components according to the addition rule (pure GO starts weight loss around  $600^\circ\text{C}$ ) (Gómez et al., 2013). Fig. 2b shows the DTG curves. Each sample presents a well-defined maximum degradation speed. The  $T_{max\ deg}$  decreases as the CMC content increases. Additions of GO and CMC components change the final weight loss from 13% to 19–20% accordingly.

### 3.3. Dielectric relaxation spectroscopy characterization

The dielectric spectra of the dried BC/CMC/GO samples show two zones related to the microscopic fluctuations of the molecular dipoles (dipolar relaxations) and charges transport across the samples (conductive processes). An isochronal representation of the data has been chosen for the sake of clarity. Fig. 3a displays the temperature dependence of the dielectric permittivity ( $\epsilon'$ ) and loss permittivity ( $\epsilon''$ ) of the dried BC/CMC/GO samples at  $10^2$  Hz. The  $\epsilon'$  spectrum presents two zones. At low temperatures a step associated with the dipolar processes is displayed, while at higher temperatures a significant increase of the permittivity related to the electrode polarization (EP) effect is observed. Additionally, the  $\epsilon''$  spectrum shows different relaxation zones. At a low temperature, an ambiguous process ( $\gamma$ -relaxation) merges as a shoulder of the main process ( $\beta$ -relaxation). Unfortunately, the  $\gamma$ -relaxation falls on the low temperature limit for measurements, making the subsequent analysis difficult. By increasing the order of temperature, the loss isochrones present a dominant absorption labelled as  $\beta$ -relaxation, which is observed for all samples studied. The intensity of the  $\beta$ -relaxation observed between  $-120^\circ\text{C}$  and  $-50^\circ\text{C}$  decreases significantly by increasing CMC concentration. As for other dried cellulose materials, the primary  $\alpha$ -relaxation directly connected to glass transition was not observed (Einfeldt, Meißner, Kwasniewski, Einfeldt, 2001; Einfeldt, Meißner, Kwasniewski, 2001; Einfeldt et al., 2004). One possible explanation of this fact could be the low amorphous content due to the high crystallinity of the BC. In the second zone, the conductive processes dominate the dielectric response. The processes include the migration of mobile charge carriers across the medium (ohmic conduction or electronic conduction) and the trapping of charges at interfaces and boundaries (non-ohmic conduction or polarization effects).

For the convenience of further analysis, the dielectric loss was also plotted in the frequency domain. One dominant relaxation ( $\beta$ -peak) between  $-150^\circ$ – $0^\circ\text{C}$  appears. For the sake of clarity, the dielectric loss of one isotherm ( $-90^\circ\text{C}$ ) of the five studied samples is shown in Fig. 3b. From this plot, one may imply that the position of the  $\beta$ -peak is scarcely affected by the CMC concentration. However, as CMC concentration increases, the  $\beta$ -peak tends to (i) slightly increase in broadness (see inset Fig. 3b) and (ii) significantly decrease in intensity.

In order to characterize the  $\beta$ -process observed in the spectra of all analyzed samples, the empirical HN (Havriliak & Negami, 1966; Havriliak & Havriliak, 1967) model has been used. The HN fitting parameters were determined at several temperatures from a multiple nonlinear regression analysis of the experimental data. Due to the symmetry of the secondary absorptions, the value of the  $b_{HN}$  parameter was fixed to 1 in the fitting procedure.

The temperature dependence of  $\Delta\epsilon_\beta$ , displayed in Fig. 4a, shows that in the range of temperature analyzed, this parameter is nearly constant. Nevertheless, a significant change was observed in the  $\Delta\epsilon_\beta$  between samples in which BC was incubated in the presence or absence of CMC. By plotting the CMC content dependence of  $\Delta\epsilon_\beta$  obtained at  $-90^\circ\text{C}$ , an inverse relationship between both parameters is observed (inset Fig. 4a), probably due to the fact that

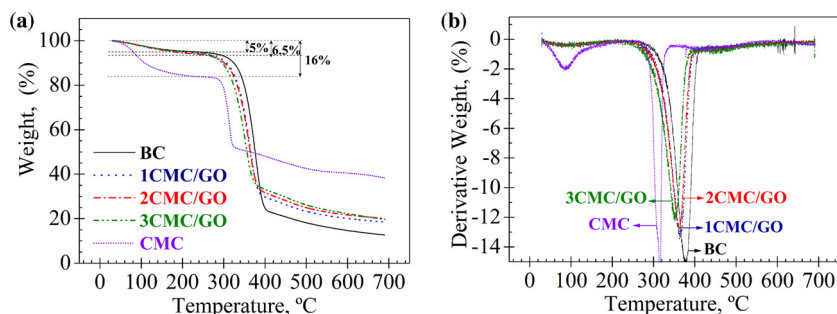


Fig. 2. Curves of weight as function temperature (a) and derivative weight % as function of temperature (b) from the TGA tests of BC composites.

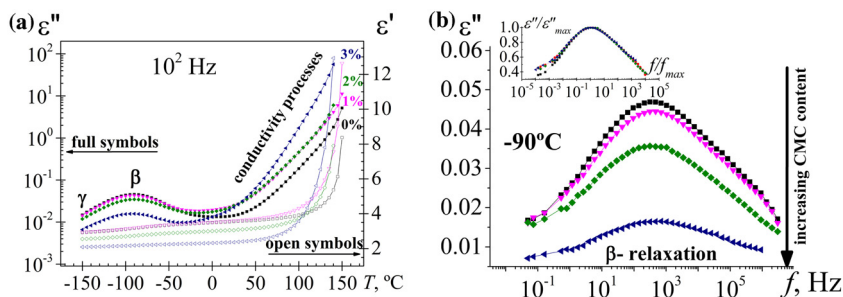


Fig. 3. (a) Temperature dependence of the dielectric permittivity at  $10^2$  Hz and (b) frequency dependence of loss permittivity at  $-90$  °C for the BC/CMC/GO analyzed samples. Inset: Normalized plot. (BC: square, 1CMC/GO: triangle down, 2CMC/GO: diamond, 3CMC/GO triangle left).

Table 2

Characteristic parameters of Arrhenius fit corresponding to the  $\beta$  and conductive processes.

sample	$\beta$ -process		Conductive process	
	$\log_{10} \tau_0$	$E_a$ (kJ/mol)	$\ln \sigma_0$	$E_a$ (kJ/mol)
BC	$-15.1 \pm 0.2$	$40.9 \pm 0.3$	$8.1 \pm 0.8$	$113.6 \pm 2.6$
1CMC/GO	$-15.2 \pm 0.1$	$41.0 \pm 0.2$	$11.4 \pm 0.4$	$119.9 \pm 1.2$
2CMC/GO	$-14.8 \pm 0.1$	$39.7 \pm 0.2$	$12.8 \pm 0.80$	$118.3 \pm 2.5$
3CMC/GO	$-14.2 \pm 0.1$	$37.3 \pm 0.2$	$13.1 \pm 0.6$	$115.0 \pm 1.9$

CMC presence promotes a structural change in the BC as has been reported previously (Watanabe, Tabuchi, Morinaga, & Yoshinaga, 1998; Yamamoto, Horii, & Odani, 1989; Yamamoto, Horii, & Hirai, 1996). This structural change, involves a variation in inter- and intramolecular interactions (hydrogen-bonding interactions), and thus, subsequent variation in the molecular mobility of the composite. Hence, the term  $N_p \mu_0^2 g \beta$  in the Onsager–Fröhlich–Kirkwood (OFK) equation (Fröhlich, 1959) that depends on the dipolar reorientation of  $N$  identical molecules per volume unit, probably is reduced by increasing the CMC content.

The temperature dependence of the width parameter is plotted in Fig. 4b. For all samples, the  $a_{HN}$  shape parameter increases linearly with temperature from 0.21 to 0.28. The low value obtained for this parameter indicates that the  $\beta$ -relaxation is a very distributed process.

The temperature dependence of  $\tau_{HN}$  is shown in Fig. 4c. It can be seen that the process for all samples follows ARR behavior,  $\tau_{HN} = \tau_0 \exp [E_a/RT]$ . Their activation energies ( $E_a$ ) and pre-exponential factors ( $\tau_0$ ) are summarized in Table 2. Both quantities represent two different effects: (i) energetic effect ( $E_a$ ) and (ii) entropic effect,  $S_a \approx -R \cdot \ln (\tau_0/\tau_D)$ , where  $S_a$  is the excess entropy of the reorientation process of the dipole system taking place during the dielectric polarization and  $\tau_D = h/k_B T_0 = 1.7 \times 10^{-13}$  s is the Debye relaxation time (Starkweather, 1991). With rising CMC concentration, both  $E_a$  and  $S_a$  values slightly decrease (inset Fig. 4c). The activation energies were found to lie between 41 and 37 kJ/mol

and the pre-exponential factor between  $10^{-15}$  and  $10^{-14}$  s. The  $E_a$  values are similar to those reported for cellulose (46 kJ/mol) and for BC (45 kJ/mol) (Einfeldt, Meißner, Kwasniewski, 2001; Grande et al., 2008).

With the goal of characterizing the conductive behavior, it is advisable to plot the obtained dielectric data in terms of the complex conductivity related to the complex dielectric permittivity as  $\sigma^*(\omega) = i \cdot \omega \cdot \epsilon_0 \cdot \epsilon^*(\omega)$ , where  $\epsilon_0$  is the vacuum permittivity. As usual, in the frequency domain, the isotherms corresponding to low temperatures of the real component of the conductivity ( $\sigma'$ ) show a nearly linear dependence with frequency (Jonscher, 1977). However, isotherms corresponding to higher temperatures, display a plateau in the low frequency region, reflecting frequency independent conductivity, i.e., dc conductivity ( $\sigma_{dc}$ ), attributed to resistive conduction through the polymer bulk. The  $\sigma_{dc}$  increases by increasing CMC concentration. So, this result indicates that the BC structural changes, promoted by the presence of CMC, enhance the conduction through the polymer bulk. Fig. 5 clearly conveys this effect, displaying the conductivity spectra of the BC/CMC/GO samples analyzed at  $140$  °C. The presence of GO and CMC clearly produces a rise in conductivity (Fig. 5). In addition, the EP, associated with the accumulation of charges at the electrode-sample interface, is enhanced by increased CMC concentration (inset of Fig. 5). This effect can be related to the increase of ion charge produced by increasing the CMC sodium salt concentration. The temperature dependence of the  $\sigma_{dc}$ , obtained from extrapolations at low frequencies, can be described by an ARR relationship. The fit parameters ( $E_a$  and  $\sigma_0$ ) obtained are summarized in Table 2. A slight reduction of the  $E_a$  with CMC concentration was once again observed.

### 3.4. X-ray diffraction

The structural order of BC/CMC/GO samples is expected to influence the thermal and dielectric properties. For this reason, it is pertinent to carry out a XRD study of our samples in order to

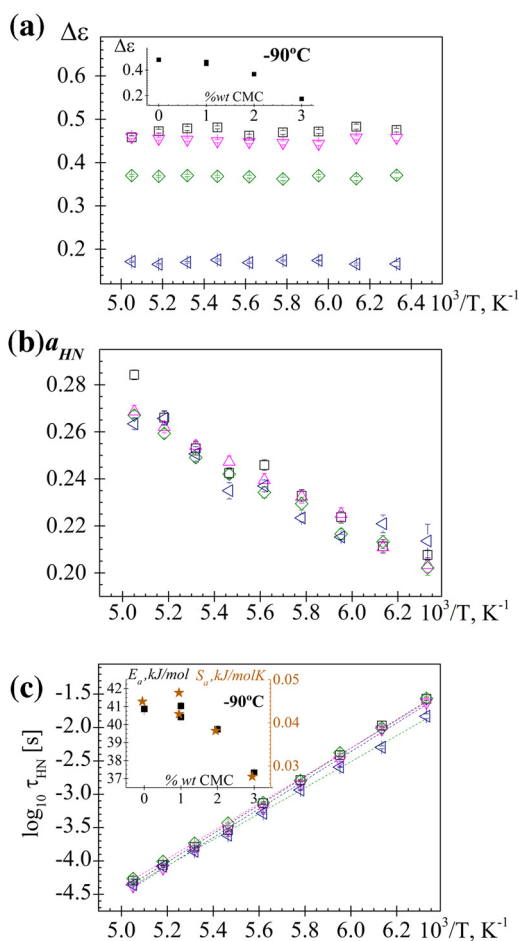


**Fig. 4.** Temperature and CMC content dependence of (a)  $\Delta\epsilon_{\beta}$  (inset: CMC content dependence of  $\Delta\epsilon_{\beta}$  at  $-90^{\circ}\text{C}$ ), (b)  $a_{HN}$  and (c)  $\tau_{HN\beta}$  inset: CMC content dependence of  $E_{\alpha}$  (kJ/mol) [square] and  $S_{\alpha}$  (kJ/(mol K)) [star] at  $-90^{\circ}\text{C}$ . BC: square, 1CMC/GO: triangle down, 2CMC/GO: diamond, 3CMC/GO triangle left.

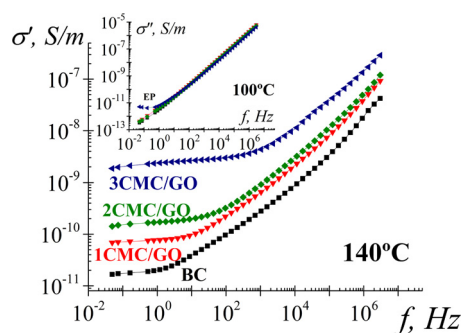


**Fig. 5.** Frequency dependence of the  $\sigma'$  for BC/CMC/GO samples at  $140^{\circ}\text{C}$ . Inset: Frequency dependence of the  $\sigma''$  at  $100^{\circ}\text{C}$ .

establish correlation between structural, thermal and dielectric properties.

The XRD patterns obtained for BC/CMC/GO composites and pure BC are shown in Fig. 6. The sharp peaks indicate that the BC is semicrystalline, as has previously been reported (Klemm, Heublein, Fink, & Bohn, 2005). All patterns show three diffraction peaks at  $2\theta$  near  $14.4^{\circ}$  ( $d_1$ ),  $16.7^{\circ}$  ( $d_2$ ) and  $22.5^{\circ}$  ( $d_3$ ). These peaks can be attributed to the (100), (010) and (110) planes of cellulose  $I_{\alpha}$  or the (1 $\bar{1}$ 0), (110) and (200) of cellulose  $I_{\beta}$  (French, 2014). Analysis of the three diffraction peaks was carried out to determine the  $d$ -spacing,

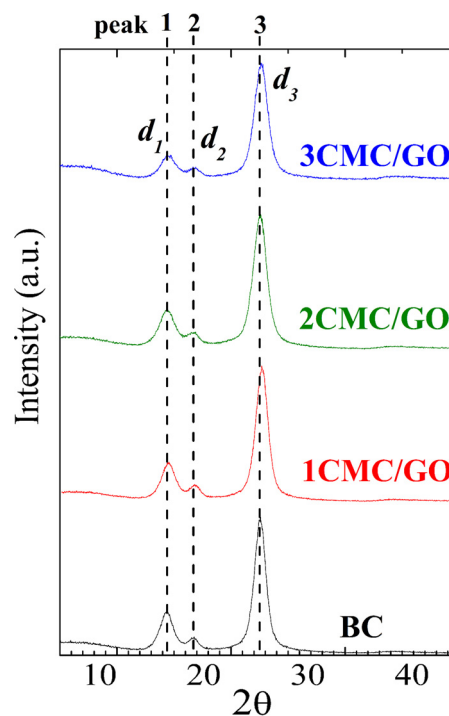


**Fig. 6.** X-ray diffractometry profiles of BC/CMC/GO samples.

**Table 3**

$d$ -spacing, crystallite sizes ( $L$ ),  $I_{\alpha}/I_{\beta}$ , and crystallite index (CrI) of samples analyzed.

	BC	1CMC/GO	2CMC/GO	3CMC/GO
$d$ -spacing (nm)	$d_1$	0.617	0.618	0.615
	$d_2$	0.533	0.534	0.533
	$d_3$	0.394	0.395	0.395
$L$ (nm)	6.46	6.13	5.46	5.65
$(I_{\alpha}/I_{\beta})^a$	–	–	0.98/0.02	0.74/0.26
CrI <sup>b</sup> (%)	96.2	95.8	94.8	

<sup>a</sup> Wada et al., 2003:  $f_{\beta X\text{-Ray}} = -70.542 \cdot d_1 + 37.583 \cdot d_2 + 23.360$ .

<sup>b</sup> CrI Segal.

the crystallite sizes ( $L$ ),  $I_{\alpha}/I_{\beta}$ , and crystallite index (CrI) of each peak of the samples studied, as summarized in Table 3.

The intensity of the  $d_1$ -spacing is higher than the  $d_2$ -spacing, which is characteristic of typical cellulose samples that contain mostly  $I_{\alpha}$  phase (Lee et al., 2015; Tokoh et al., 1998). Nevertheless, by increasing the CMC content, the difference between the intensity of both peaks is reduced. On the other hand, the difference between the Bragg angle of peak 1 ( $d_1$ ) and peak 2 ( $d_2$ ), decreases with an increased CMC content. This fact suggests that increasing the CMC content decreases the cellulose  $I_{\alpha}$  phase fraction (Watanabe et al., 1998; Yamamoto et al., 1989, 1996). Wada et al. (Wada, Kondo, & Okano, 2003) have proposed a method to estimate the  $I_{\beta}$  fraction of the sample from the  $d$ -spacing ( $d_1$ ,  $d_2$ ). According to our results, the mass fraction of cellulose  $I_{\alpha}$  is greatly decreased with an increasing concentration of CMC. So, the positions of the XRD peaks change with CMC concentration due to the varying  $I_{\alpha}/I_{\beta}$  ratio in the samples.

The CrI values evaluated Segal (Segal et al., 1962) procedure decrease as the CMC concentration increases (Table 3). The  $\Delta\epsilon_{\beta}$  and the CrI values obtained for BC samples are in agreement with those reported by Einfeldt et al. (Einfeldt et al., 2004).

The shape and size of crystallites can affect the obtained CrI values. Cellulose crystallites with a square cross sectional shape should have nearly equal intensities of the  $d_1$  (peak 1) and  $d_2$  (peak 2) spacings (Moon, Martini, Nairn, Simonsen, & Youngblood, 2011).

The slightly stronger  $d_1$  reflection in Fig. 6 indicates that cellulose crystallites are of rectangular shape.

The crystal size,  $L$ , estimated from peak 3 ( $d_3$ ), decreases from 6.46 nm to 5.65 nm as the concentration of CMC increases (Table 3). This harmoniously decrease agrees with the decrease in average microfibril size and the change of packing density obtained from SEM and AFM observations. At the same time it agrees with the thermal stability range of the samples obtained by TGA. Thus, according to Poletto et al. (Poletto et al., 2013) higher CrI and  $L$  is related to a higher thermal stability, but for the same CrI, the order of the different crystallites can affect the thermal stability (Poletto et al., 2014). Additionally, we should consider that further degradation of the CMC component may favor the degradation of the BC component.

#### 4. Conclusions

This work presents a combined analysis of the structure and properties of cellulose bacterial composites reinforced by graphene oxide. As a result, the crucial role of CMC addition to induce substantial structural changes in Cellulose is evidenced. The fraction of the two allomorphs of I structure ( $I_{\alpha}/I_{\beta}$ ) is greatly decreased with increasing concentrations of CMC sodium salt (CMC) in the incubation medium. The crystalline size and crystallinity sample index decrease with an increasing concentration of CMC. The sample CrI values, estimated from the ratio of the area of the crystalline peaks to the total area, experiences a reduction of a 13% with respect BC alone. These changes in the sample's CrI value and morphology are in good agreement with the results obtained from SEM and AFM.

The proportion of both phases and how they are distributed in the microfibrils determines electrical behavior and therefore, their potential applications. As expected, the presence of GO produces a rise in the conductivity of the BC composites. Additionally, this increase is higher with increasing the CMC content. The dynamic mobility is dramatically affected by the number of hydroxyl groups and their ability to make hydrogen bonds between cellulose chains. Both the  $\beta$ -relaxation and conductivity process are thermally activated processes, and both are steeply dependent on the CMC concentration.

Given the results obtained, we believe that the composites described herein could find various applications in portable and bendable electronics. According to our results the sample with a 3% of CMC has the higher conductivity, but it would be appropriate to perform a future study of samples with higher GO and CMC contents, in order to find the composition that optimizes the electric properties.

#### Acknowledgements

This work was supported by the DGCYT [MAT2015-63955-R]; the Vice-Rectorate for Research of the Pontificia Universidad Católica del Perú and the National Council of Science, Technology and Technological Innovation of Peru (CONCYTEC/FONDECYT).

#### References

- Ahvenainen, P., Kontro, I., & Svedström, K. (2016). Comparison of sample crystallinity determination methods by X-ray diffraction for challenging cellulose I materials. *Cellulose*, 23, 1073–1086.
- Alexander, L. E. (1979). X-ray diffraction methods in polymer science. In R. E. Krieger (Ed.), (pp. 423–424). New York: Krieger.
- Atalla, R. H., & Vanderhart, D. L. (1984). Native cellulose: A composite of two distinct crystalline forms. *Science*, 223, 283–285.
- Bansal, P., Hall, M., Realf, M. J., Lee, J. H., & Bommarius, A. S. (2010). Multivariate statistical analysis of X-ray data from cellulose: A new method to determine degree of crystallinity and predict hydrolysis rates. *Bioresource Technology*, 101(12), 4461–4471.
- Bohn, A., Fink, H. P., Ganster, J., & Pinnow, M. (2000). X-ray texture investigations of bacterial cellulose. *Macromolecular Chemistry and Physics*, 201(15), 1913–1921.
- Chen, H. H., Chen, L. C., Huang, H. C., & Lin, S. B. (2011). In situ modification of bacterial cellulose nanostructure by adding CMC during the growth of *Gluconacetobacter xylinus*. *Cellulose*, 18(6), 1573–1583.
- Chen, D., Feng, H., & Li, J. (2012). Graphene oxide: Preparation, functionalization, and electrochemical applications. *Chemical Reviews*, 112(11), 6027–6053.
- Dayal, M. S., & Catchmark, J. M. (2016). Mechanical and structural property analysis of bacterial cellulose composites. *Carbohydrate Polymers*, 144, 447–453.
- Ebrahimzadeh, S., Ghanbarzadeh, B., & Hamishehkar, H. (2016). Physical properties of carboxymethyl cellulose based nano-biocomposites with graphene nano-platelet. *International Journal of Biological Macromolecules*, 84, 16–23.
- Einfeldt, J., & Kwasniewski, A. (2002). Characterization of different types of cellulose by dielectric spectroscopy. *Cellulose*, 9, 225–238.
- Einfeldt, J., Meißner, D., Kwasniewski, A., & Einfeldt, L. (2001). Dielectric spectroscopic analysis of wet and well dried starches in comparison with other polysaccharide. *Polymer*, 42, 7049–7062.
- Einfeldt, J., Meißner, D., & Kwasniewski, A. (2001). Polymer dynamics of cellulose and other polysaccharides in solid state—secondary dielectric relaxation processes. *Progress in Polymer Science*, 26, 1419–1472.
- Einfeldt, J., Meißner, D., & Kwasniewski, A. (2004). Molecular interpretation of the main relaxations found in dielectric spectra of cellulose—experimental arguments. *Cellulose*, 11, 137–150.
- Fan, H., Wang, L., Zhao, K., Li, N., Shi, Z., Ge, Z., et al. (2010). Fabrication, mechanical properties: And biocompatibility of graphene-reinforced chitosan composites. *Biomacromolecules*, 11, 2345–2351.
- Feng, Y., Zhang, X., Shen, Y., Yoshino, K., & Feng, W. (2012). A mechanically strong: Flexible and conductive film based on bacterial cellulose/graphene nanocomposite. *Carbohydrate Polymers*, 87, 644–649.
- Frohlich, H. (1959). *Theory of dielectrics* (2nd ed.). Oxford: Oxford University Press.
- French, A. D. (2014). Idealized powder diffraction patterns for cellulose polymorphs. *Cellulose*, 21, 885–896.
- Gómez, C. M., Culebras, M., Cantarero, A., Redondo-Foj, B., Ortiz-Serna, P., Carsí, M., et al. (2013). An experimental study of dynamic behaviour of graphite–polycarbonatediol polyurethane composites for protective. *Coatings Applied Surface Science*, 275, 295–302.
- Gómez-Navarro, C., Meyer, J. C., Sundaram, R. S., Chuvilin, A., Kurasch, S., Burghard, M., et al. (2010). Atomic structure of reduced graphene oxide. *Nano Letters*, 10(4), 1144–1148.
- Gelin, K., Bodin, A., Gatenholm, P., Mihranyan, A., Edwards, K., & Strømme, M. (2007). Characterization of water in bacterial cellulose using dielectric spectroscopy and electron microscopy. *Polymer*, 48, 7623–7631.
- Grande, C. J., Torres, F. G., Gomez, C. M., Troncoso, O. P., Canet-Ferrer, J., & Martínez-Pastor, J. (2008). Morphological characterisation of bacterial cellulose–starch nanocomposites. *Polymers & Polymer Composites*, 16(3), 181–185.
- Grande, C. J., Torres, F. G., Gomez, C. M., & Bañó, M. C. (2009). Nanocomposites of bacterial cellulose/hydroxyapatite for biomedical applications. *Acta Biomaterialia*, 5(5), 1605–1615.
- Grande, C. J., Torres, F. G., Gomez, C. M., Troncoso, O. P., Canet-Ferrer, J., & Martínez-Pastor, J. (2009). Development of self-assembled bacterial cellulose–starch nanocomposites. *Materials Science and Engineering: C*, 29(4), 1098–1104.
- Gu, J., & Catchmark, J. M. (2012). Impact of hemicelluloses and pectin on sphere-like bacterial cellulose assembly. *Carbohydrate Polymers*, 88, 547–557.
- Han, D., Yan, L., Chen, W., Li, W., & Bangal, S. J. (2011). Cellulose/graphite oxide composite films with improved mechanical properties over a wide range of temperature. *Carbohydrate Polymers*, 83(2), 966–972.
- Havriliak, S., & Havriliak, S. (1967). *Dielectric and mechanical relaxation in materials*. Munich: Hanser.
- Havriliak, S., & Negami, S. (1966). A complex plane analysis of  $\alpha$ -dispersions in some polymer systems. *Journal of Polymer Science Polymer Symposia*, 14, 99–117.
- Hermans, P. H., & Weidinger, A. (1949). X-ray studies on the crystallinity of cellulose. *Journal of Polymer Science*, 4, 135–144.
- Hirai, F., Yamamoto, H., & Hirai, A. (1997). Microstructural analysis of microfibrils of bacterial cellulose. *Macromolecular Symposia*, 120, 197–205.
- Huang, H. C., Chen, L. C., Lin, S. B., Hsu, C. P., & Chen, H. H. (2010). In situ modification of bacterial cellulose network structure by adding interfering substances during fermentation. *Bioresource Technology*, 101(15), 6084–6091.
- Iguchi, M., Yamanaka, S., & Budhiono, A. (2000). Bacterial cellulose: A masterpiece of nature's arts. *Journal of Materials Science*, 35(2), 261–270.
- Jonscher, A. K. (1977). The 'universal' dielectric response. *Nature*, 267, 673–679.
- Kafy, A., Sadasivuni, K. K., Kim, H. C., Akther, A., & Kim, J. (2015). Designing flexible energy and memory storage materials using cellulose modified graphene oxide nanocomposites. *Physical Chemistry Chemical Physics*, 17(8), 5923–5931.
- Kamarudin, K. H., & Isa, M. I. N. (2013). Structural and DC ionic conductivity studies of carboxy methylcellulose doped with ammonium nitrate as solid polymer electrolytes. *International Journal of Physical Sciences*, 8(31), 1581–1587.
- Kim, J., Cai, Z., Lee, H. S., Choi, G. S., Lee, D. H., & Jo, C. (2011). Preparation and characterization of a bacterial cellulose/chitosan composite for potential biomedical application. *Journal of Polymer Research*, 18, 739–744.
- Kim, C. J., Khan, W., Kim, D. H., Cho, K. S., & Park, S. Y. (2011). Graphene oxide/cellulose composite using NMMO monohydrate. *Carbohydrate Polymers*, 86(2), 903–909.
- Klemm, D., Heublein, B., Fink, H. P., & Bohn, A. (2005). Cellulose: Fascinating biopolymer and sustainable raw material. *Angewandte Chemie International Edition*, 44, 3358–3393.

- Kremer, F., & Schönhal, A. (2003). *In broadband dielectric spectroscopy*. Berlin: Springer.
- Lee, C. M., Gu, J., Kafle, K., Catchmark, J., & Kim, S. H. (2015). Cellulose produced by *Gluconacetobacter xylinus* strains ATCC 53524 and ATCC 23768: Pellicle formation post-synthesis aggregation and fiber density. *Carbohydrate Polymers*, *133*, 270–276.
- Lin, W. C., Lien, C. C., Yeh, H. J., Yu, C. M., & Hsu, S. H. (2013). Bacterial cellulose and bacterial cellulose–chitosan membranes for wound dressing applications. *Carbohydrate Polymers*, *94*, 603–611.
- Liu, Y., Yu, D., Zeng, C., Miao, Z., & Dai, L. (2010). Biocompatible graphene oxide-based glucose biosensors. *Langmuir*, *26*(9), 6158–6160.
- Liu, Y., Zhou, J., Zhu, E., Tang, J., Liu, X., & Tang, W. (2015). Facile synthesis of bacterial cellulose fibres covalently intercalated with graphene oxide by one-step cross-linking for robust supercapacitors. *Journal of Materials Chemistry C*, *3*(5), 1011–1017.
- Luong, N. D., Pahimanolis, N., Hippo, U., Korhonen, J. T., Ruokolainen, J., Johansson, L.-S., et al. (2011). Graphene/cellulose nanocomposite paper with high electrical and mechanical performances. *Journal of Materials Chemistry*, *21*, 13991–13998.
- Miyachi, M., Miao, J., Simmons, T. J., Lee, J.-W., Doherty, T. V., Dordick, J. S., et al. (2010). Conductive cable fibers with insulating surface prepared by coaxial electrospinning of multiwalled nanotubes and cellulose. *Biomacromolecules*, *11*, 2440–2445.
- Mohite, B., & Patil, S. V. (2016). Cellulose and cellulose derivatives synthesis, modification and applications. In M. D. Ibrahim, & H. Mondal (Eds.), *Chapter: Insights into bacterial cellulose biosynthesis and production* (pp. 27–48). New York: Nova Publishers.
- Moon, R. J., Martini, A., Nairn, J., Simonsen, J., & Youngblood, J. (2011). Cellulose nanomaterials review: Structure, properties and nanocomposites. *Chemical Society Reviews*, *40*, 3941–3994.
- Nakagaito, A. N., Iwamoto, S., & Yano, H. (2005). Bacterial cellulose: The ultimate nano-scalar cellulose morphology for the production of high-strength composites. *Applied Physics A*, *80*(1), 93–97.
- Nishiyama, Y. (2009). Structure and properties of the cellulose microfibril. *Journal of Wood Science*, *55*, 241–249.
- O'Sullivan, A. C. (1977). Cellulose: The structure slowly unravels. *Cellulose*, *4*, 173–207.
- Park, S., Baker, J. O., Himmel, M. E., Parilla, P. A., & Johnson, D. K. (2010). Cellulose crystallinity index: Measurement techniques and their impact on interpreting cellulose performance. *Biotechnology for Biofuels*, *3*, 1–10.
- Poletto, M., Pistor, V., & Zattera, A. J. (2013). Structural characteristics and thermal properties of native cellulose, cellulose-fundamental aspects. In T. van de Ven, & L. Godbout (Eds.), *InTech*, 10.5772/2705.
- Poletto, M., Ornaghi, H. L., Jr, & Zattera, A. J. (2014). Native cellulose: Structure characterization and thermal properties. *Materials*, *7*, 6105–6119.
- Riande, E., & Díaz-Calleja, R. (2004). *Electrical properties of polymers*. New York: Dekker.
- Sadasivuni, K. K., Kafy, A., Zhai, L., Ko, H. U., Mun, S., & Kim, J. (2015). Transparent and flexible cellulose nanocrystal/reduced graphene oxide film for proximity sensing. *Small*, *11*(8), 994–1002.
- Segal, L., Creely, J. J., Martin, A. E., Jr., & Conrad, C. M. (1962). An empirical method for estimating the degree of crystallinity of native cellulose using the x-ray diffractometer. *Textile Research Journal*, *29*, 786–794.
- Shao, W., Liu, H., Liu, X., Wang, S., & Zhang, R. (2015). Anti-bacterial performances and biocompatibility of bacterial cellulose/graphene oxide composites. *RSC Advances*, *5*, 4795.
- Shao, W., Wang, S., Liu, H., Wu, J., Zhang, R., Minc, H., et al. (2016). Preparation of bacterial cellulose/graphene nanosheets composite films with enhanced mechanical performances. *Carbohydrate Polymers*, *138*, 166–171.
- Si, H., Luo, H., Xiong, G., Yang, Z., Raman, S. R., Guo, R., et al. (2014). One-step In situ biosynthesis of graphene oxide–bacterial cellulose nanocomposite hydrogels. *Macromolecular Rapid Communications*, *35*, 1706.
- Starkweather, H. W., Jr. (1991). Aspects of simple non-cooperative relaxations. *Polymer*, *32*(13), 2443–2448.
- Terinte, N., Ibbett, R., & Schuster, K. C. (2011). On native cellulose and microcrystalline cellulose I structure studied by X-ray diffraction (Waxd): comparison between measurement techniques. *Lenzinger Berichte*, *89*, 118–131.
- Terzopoulou, Z., Kyzas, G. Z., & Bikiaris, D. N. (2015). Recent advances in nanocomposites materials of graphene derivatives with polysaccharide. *Materials*, *8*, 652–683.
- Tian, M., Qu, L., Zhang, X., Zhang, K., Zhu, S., Guo, X., et al. (2014). Enhanced mechanical and thermal properties of regenerated cellulose/graphene composite fibers. *Carbohydrate Polymers*, *111*, 456–462.
- Tokoh, C., Takabe, K., Fujita, M., & Saiki, H. (1998). Cellulose synthesized by *Acetobacter xylinum* in the presence of acetyl glucosaminan. *Cellulose*, *5*, 249–261.
- Ul-Islam, M., Khan, T., & Park, J. K. (2012). Water holding and release properties of bacterial cellulose obtained by in situ and ex situ modification. *Carbohydrate Polymers*, *88*(2), 596–603.
- Wada, M., & Okano, T. (2001). Localization of  $I_{\alpha}$  and  $I_{\beta}$ : phases in algal cellulose revealed by acid-treatments. *Cellulose*, *8*, 183–188.
- Wada, M., Kondo, T., & Okano, T. (2003). Thermally induced crystal transformation from cellulose  $I_{\alpha}$  to  $I_{\beta}$ . *Polymer Journal*, *35*(2), 155–159.
- Watanabe, K., Tabuchi, M., Morinaga, Y., & Yoshinaga, F. (1998). Structural features and properties of bacterial cellulose produced in agitated culture. *Cellulose*, *5*, 187–200.
- Watanabe, A., Morita, S., & Ozaki, Y. (2006). Study on temperature-dependent changes in hydrogen bonds in cellulose  $I_{\beta}$  by infrared spectroscopy with perturbation–correlation moving–window two-dimensional correlation spectroscopy. *Biomacromolecules*, *7*, 3164–3170.
- Watanabe, A., Morita, S., & Ozaki, Y. (2007). Temperature-Dependent changes in hydrogen bonds in cellulose  $I_{\alpha}$  studied by infrared spectroscopy in combination with perturbation–correlation moving–window two-dimensional correlation spectroscopy: Comparison with cellulose  $I_{\beta}$ . *Biomacromolecules*, *8*, 2969–2975.
- Xu, C., Wang, G., Xing, C., Matuana, L. M., & Zhou, H. (2015). Effect of graphene oxide treatment on the properties of cellulose nanofibril films made of banana petiole fibers. *BioResources*, *10*(2), 2809–2822.
- Yadav, M., Rhee, K. Y., & Park, S. J. (2013). Synthesis and characterization of graphene oxide/carboxymethylcellulose/alginate composite blend films. *Carbohydrate Polymers*, *110*, 18–25.
- Yamamoto, H., Horii, F., & Odani, H. (1989). Structural changes of native cellulose crystals induced by annealing in aqueous alkaline and acidic solutions at high temperatures. *Macromolecules*, *22*, 4132–4134.
- Yamamoto, H., Horii, F., & Hirai, A. (1996). In situ crystallization of bacterial cellulose II: Influences of different polymeric additives on the formation of celluloses  $I_{\alpha}$  and  $I_{\beta}$  at the early stage of incubation. *Cellulose*, *3*, 229–242.
- Ye, Y.-S., Zeng, H.-X., Wu, J., Dong, L.-Y., Zhu, J.-T., Xue, Z.-G., et al. (2016). Biocompatible reduced graphene oxide sheets with superior water dispersibility stabilized by cellulose nanocrystals and their polyethylene oxide composites. *Green Chemistry*, *18*, 1674–1681.